Seismic Waveform-Coherence Controlled by Earthquake Source Dimensions

Tong Zhou, Lingsen Meng, Ailin Zhang, Jean Paul Ampuero

JGR Solid Earth

RESEARCH ARTICLE
10.1029/2021JB023458

Seismic Waveform-Coherence Controlled by Earthquake Source Dimensions

Tong Zhou[1,2], Lingsen Meng[1], Ailin Zhang[3], and Jean-Paul Ampuero[4]

[1]Earth, Planetary and Space Sciences, University of California, Los Angeles, CA, USA, [2]Now at Aramco Research Center - Beijing, Aramco Asia, Beijing, China, [3]University of Michigan-Shanghai Jiao Tong University Joint Institute, Shanghai Jiao Tong University, Shanghai, China, [4]Observatoire de la Côte d'Azur, Université Côte d'Azur, IRD, CNRS, Géoazur, Valbonne, France

Key Points:

- Waveform coherence decays as a function of interstation distance faster for large earthquakes (Mw > 7)
- The waveform coherence pattern is governed by earthquake source size
- Rupture sizes inferred from waveform coherence satisfy empirical scaling relations

Supporting Information:

Supporting Information may be found in the online version of this article.

Correspondence to:

L. Meng and T. Zhou,
meng@epss.ucla.edu;
tzhou@epss.ucla.edu

Citation:

Zhou, T., Meng, L., Zhang, A., & Ampuero, J.-P. (2022). Seismic waveform-coherence controlled by earthquake source dimensions. *Journal of Geophysical Research: Solid Earth*, *127*, e2021JB023458. https://doi.org/10.1029/2021JB023458

Received 18 OCT 2021
Accepted 19 APR 2022

Author Contributions:

Conceptualization: Tong Zhou, Lingsen Meng, Jean-Paul Ampuero
Formal analysis: Tong Zhou
Funding acquisition: Lingsen Meng
Methodology: Tong Zhou, Ailin Zhang
Project Administration: Lingsen Meng
Resources: Tong Zhou, Lingsen Meng
Software: Tong Zhou, Ailin Zhang
Supervision: Lingsen Meng
Validation: Tong Zhou
Visualization: Tong Zhou
Writing – original draft: Tong Zhou
Writing – review & editing: Tong Zhou, Lingsen Meng, Jean-Paul Ampuero

Abstract Rupture size is a fundamental earthquake source parameter that is challenging to infer independently from far-field seismological observations. Here, we develop a novel observational constraint on source size based on the decay rate of wavefield coherence across a seismic array. For a given earthquake, waveform coherence decays with increasing interstation distance or, more precisely, with increasing projection difference defined as the difference between the takeoff vectors associated to the two stations projected along the rupture direction. We find that coherence generally falls off with projection difference faster for earthquakes of larger magnitudes. The magnitude dependence of the coherence decay rate can be explained by a finite source effect: larger source sizes cause larger differences of phase delays between waves arriving from different parts of the rupture at different stations, hence a stronger spatial variability of the wavefield, resulting in a breakdown of waveform coherence. Assuming a 1-D Haskell's source model, the rupture size can be estimated from the coherence decay rate. We apply this method to USArray data of earthquakes in three subduction zones, the Sea of Okhotsk, South America and Japan. The source sizes inferred from the coherence decay patterns are consistent with scaling relations intermediate between width-saturated *L*-models and quasi equi-dimensional rupture models. Our observation captures a unique pattern of array waveform coherence and demonstrates the potential of utilizing waveform coherence to study earthquake source parameters.

Plain Language Summary In this paper, we observe that for a given earthquake, the similarity of the waveform (coherence) recorded by stations in a far-field array decays with increasing interstation distance. The waveform coherence generally falls off with interstation distance faster for earthquakes of larger magnitudes and therefore, larger rupture sizes. We develop a novel method using array waveform coherence to estimate the earthquake rupture size, and apply this method to USArray data of earthquakes in three geological regions: the Sea of Okhotsk, South America and Japan. The source sizes inferred from the coherence decay patterns are consistent with previous studies using different methods. According to our observation, there is a potential to infer earthquake rupture independently from far-field observations by waveform coherence.

1. Introduction

Over the last two decades, the development of large-aperture seismic arrays, such as USArray, the European seismic networks and Hi-net network, has enabled a broad spectrum of seismological studies. The dense spatial sampling of arrays has enabled significant progress in the study of Earth's interior and earthquake source, such as constraining 3-D mantle structures beneath North America (e.g., Burdick et al., 2017; Shen & Ritzwoller, 2016), detecting deep earth discontinuities (e.g., Lin et al., 2013; Poli et al., 2015), imaging the rupture processes of large earthquakes using back-projection methods (e.g., Kiser & Ishii, 2017; Meng et al., 2018), and improving earthquake detection capabilities using template matching techniques (Gibbons & Ringdal, 2006; Peng & Zhao, 2009). Coherence-based detection methods are also applied to detect nonvolcanic tremors (e.g., Obara, 2012; Shelly et al., 2007), anthropogenic signals (Riahi & Gerstoft, 2015), closely located earthquakes or tremors with nonmatching waveforms (Hawthorne & Ampuero, 2018), and source kinematics by stereometry (Mordret et al., 2020).

While array waveform coherence has been widely applied to earthquake detection, here we exploit it to constrain earthquake source parameters, in particular rupture dimensions. Current methods to study source parameters are mostly based on deterministic waveform fitting. Finite source inversions applied to teleseismic recordings to

resolve slip distributions (Ji et al., 2002) constrain rupture duration T and moment, but suffer from a strong trade-off between source size L and rupture speed V_r ($T = L/V_r$). Hawthorne et al. (2019) introduced an approach to estimate the rupture size of low frequency earthquakes from the interstation fluctuations of interevent normalized cross-spectra, a waveform coherence property controlled by differences between the apparent source time functions viewed by each station.

Here, we examine the relationship between earthquake rupture dimension and array waveform coherence, that is, the normalized cross-correlation coefficient between waveforms recorded by pairs of stations within an array. The idea of exploring array waveform coherence is originally motivated by applications of seismic array processing to imaging Earth's structure and earthquake sources. The coherence length of an array, defined as the maximum interstation distance with adequate waveform coherence, is a key constraint on array design that determines the maximum array aperture to apply a back-projection analysis to image sources or structures. Previous work indicates that waveform coherence decays dramatically with increasing interstation distance and frequency (e.g., Langston, 2014; Zerva & Zervas, 2002). In these studies based on local seismic phases, waveform incoherence mostly results from wave scattering by crustal heterogeneities. In contrast, teleseismic waveforms involve rather simple path effects, and thus provide a unique opportunity to study the effects of earthquake source properties on waveform coherence and to assess the potential of using array waveform coherence to constrain earthquake rupture sizes.

By analyzing the coherence patterns of a variety of teleseismic earthquakes recorded by the USArray, we observe that the waveform coherence decays faster with increasing interstation distance and earthquake magnitude. This magnitude dependence of the coherence decay rate can be explained by a finite source effect. From the representation theorem, the far-field body wave seismograms of a finite-fault rupture are the integral of slip rate functions distributed along the fault surface convolved with the Green's function of each fault point (Aki & Richards, 2002). The arrival times at an array of waves coming from different parts of a rupture depend on the rupture front propagation (rupture times) and on wave propagation (travel times of the Green's functions). The latter depend both on source and receiver locations. Therefore, increasing either the source size or interstation distance can cause a larger delay between waves from different parts of the source, resulting in a breakdown of waveform coherence.

The decay rate of waveform coherence is observed to satisfy a relatively simple relation under the assumption of a 1-D Haskell's source model, which has the potential to be used for estimating the rupture sizes of earthquakes with saturated seismogenic width. Moreover, it is remarkable that the waveform coherence decay rate does not depend on rupture velocity V_r, which naturally circumvents the trade-off between rupture length L and rupture velocity V_r (Ide, 2007) in methods based on teleseismic finite-fault inversion. Nevertheless, there are still questions to be solved before applying this method to general earthquakes. First, it is difficult yet significant to separate the source-induced and path/station-induced incoherent components so that the teleseismic waveform coherence will only focus on the source parameters. Second, other complex source parameters influence the teleseismic waveform coherence decay. For example, the unsaturated seismogenic width W (quasi equal-dimensional rupture), the bilateral rupture, and the aspect ratio L/W.

In this paper, we investigate the finite-source controlled waveform coherence decay in detail. First, we demonstrate the teleseismic waveform coherence pattern predicted by a 1-D Haskell's source model and find a relation between interstation waveform coherence and "projection difference", a measurement of interstation difference between takeoff vectors projected along the rupture direction. The interstation coherence falls off as a function of projection difference and earthquake rupture length. Second, we study the interstation coherence of teleseismic earthquake waveforms recorded by USArray in the Eastern United States. For a given earthquake, we find that interstation coherence decays as a function of projection difference and magnitude (related to the rupture size). Next, we estimate the rupture lengths by fitting the coherence decay rate and projection difference, and assess the uncertainty of the estimated rupture length. We investigate the moment-size scaling relationship between the coherence estimated rupture dimensions and moment magnitudes. Finally, we address the impacts of source complexities on the rupture size estimation, including finite-frequency, aspect ratio, and bilateral rupture.

2. The Elongated Haskell Source Model

To demonstrate the hypothesis that source size controls the decay pattern of interstation coherence, we establish an analytical relationship between interstation coherence and the source size of a unilateral rupture. Following Haskell (1964), we assume an elongated rectangular rupture with uniform slip, length L and width W such that

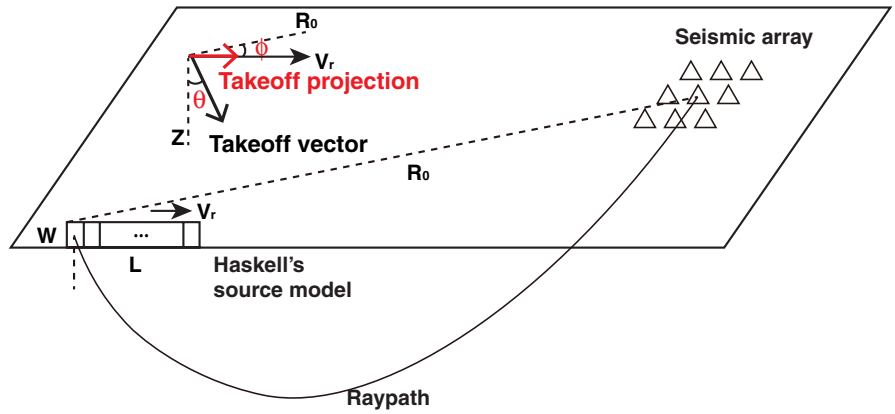

Figure 1. Conceptual description of a Haskell's source model recorded by a teleseismic array and definition of the takeoff projection.

$L \gg W$, embedded in a 3-D homogeneous elastic space, propagating unilaterally at constant rupture speed V_r along the L direction, with a uniform invariant trapezoidal slip-rate function (Figure 1). This simple setting is intended to isolate the effect of source size on waveform coherence. An array is located at the teleseismic distance R_0. For a seismic ray going from the hypocenter to a station, we denote the azimuth relative to the rupture propagation vector as ϕ and the takeoff angle as θ. We define the takeoff projection γ as the projection of the takeoff vector onto the rupture direction ($\gamma = \sin\theta\cos\phi$, red arrow in Figure 1).

The far-field displacement u at a receiver at distance r and takeoff projection γ, relative to the hypocenter, is the integral of the contributions from all points (at distance x from the hypocenter) along the rupture:

$$u(r,\gamma,t) = \frac{\mu W}{4\pi\rho c^3}\int_0^L \frac{R}{r}\dot{D}\left(t - \frac{r}{c} - \frac{x}{V_r} + \frac{\gamma x}{c}\right)\mathrm{dx}, \tag{1}$$

where c is the P wave speed, t the time, μ the rigidity, ρ the density, R the radiation pattern, and $\dot{D}$ the slip rate function. Equation 1 accounts for an integration along the rupture length L, which is assumed much smaller than the source-receiver distance. Taking the Fourier transform, we get

$$U(r,\gamma,\omega) = \frac{\mu RW}{4\pi\rho c^3 r}\dot{D}(\omega)e^{-\frac{i\omega r}{c}}\int_0^L e^{-i\omega\left(\frac{x}{V_r}-\frac{\gamma x}{c}\right)}\mathrm{dx}. \tag{2}$$

Integrating Equation 2 along the whole rupture length L, we get

$$U(r,S,\omega) = \frac{\mu RW}{4\pi\rho c^3 r}\dot{D}(\omega)e^{-\frac{i\omega r}{c}}\frac{1}{\omega S}\sin\left(\frac{\omega L}{2}S\right)e^{-\frac{i\omega L}{2}S}, \tag{3}$$

where S is a slowness term:

$$S = \frac{1}{V_r} - \frac{\gamma}{c}. \tag{4}$$

Equation 3 does not consider receiver-side scatterings and site effects. Convolving a term representing these effects $Ge^{-i\omega g}$, we get

$$U = \frac{\mu RWG}{4\pi\rho c^3 r}\dot{D}(\omega)\frac{1}{\omega S}\sin\left(\frac{\omega L}{2}S\right)\exp\left[-i\omega\left(\frac{r}{c} + \frac{LS}{2} + g\right)\right]. \tag{5}$$

The coherence spectrum between the seismograms recorded at stations A and B, defined from the normalized cross-spectrum at frequency ω, can be written as

$$\mathrm{CC}(\omega) = \frac{\mathrm{Real}\left(U\left(S_A,\omega\right)\cdot U^*\left(S_B,\omega\right)\right)}{\left|U\left(S_A,\omega\right)\right|\cdot\left|U\left(S_B,\omega\right)\right|} = \cos\left[-\frac{\omega L}{2c}\left(\gamma_A - \gamma_B\right) + \omega\left(g_A - g_B\right)\right]. \tag{6}$$

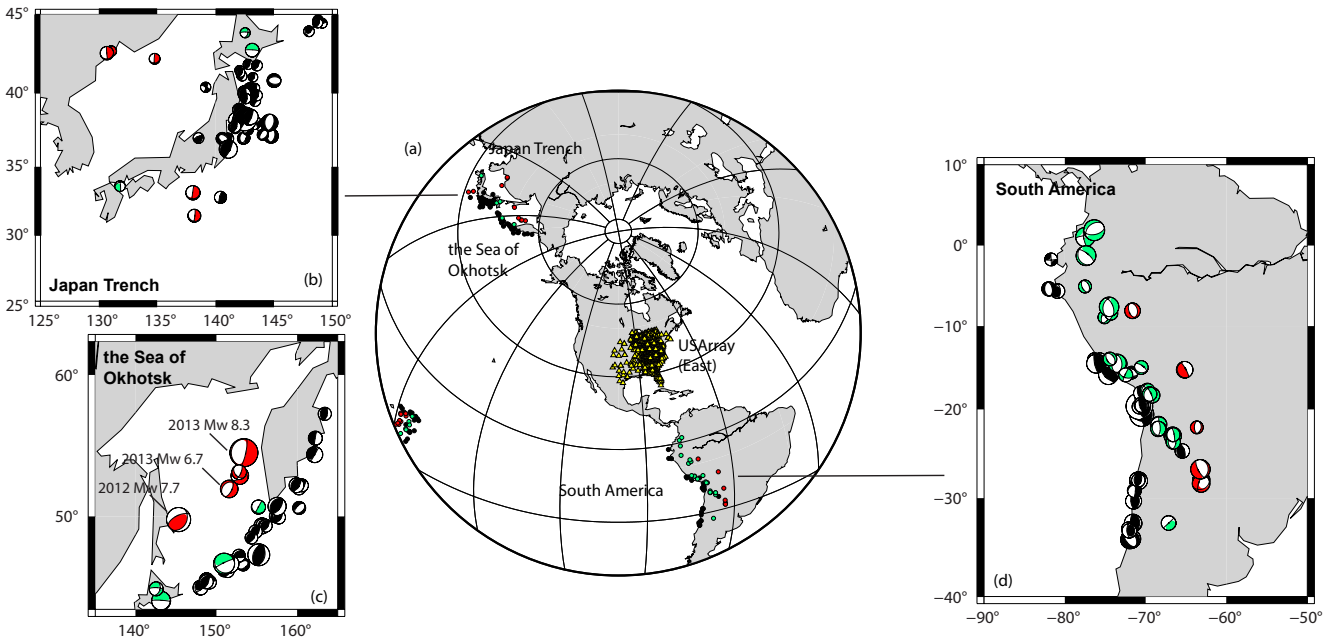

Figure 2. Array and earthquakes used in this study for waveform coherence measurement. (a) global view of earthquakes and seismic array (USArray in the Eastern United States, operating from 2011 to 2015); Selected events in (b) Japan, (c) the Sea of Okhotsk, and (d) South America subduction zone. Focal mechanisms (beach balls) and dots are color coded by depth: >300 km in red, 70–300 km in green, and <70 km in black.

The detailed derivation of Equation 6 is given in the Appendix A. We define the projection difference as the difference of takeoff projections between two stations, $d_p = \gamma_A - \gamma_B$ (Figure 1). The projection difference is related to both the interstation distance and the takeoff angle. We also define the error difference as $\delta = \omega(g_A - g_B)$, which accounts for the difference of local scatterings and site effects between the two stations. Equation 6 shows that interstation coherence is affected by three factors: the source rupture size L, the interstation projection difference (related to the interstation distance), and frequency. In particular, a larger rupture length L or increase in frequency results in a smaller coherence; therefore, faster coherence decay as a function of projection difference is expected for larger earthquakes in the same passband.

3. Measurements of Waveform-Coherence Decay Rates

Besides the 1-D unilateral Haskell's rupture model, we seek to find seismic waveform coherence decay controlled by earthquake size in real teleseismic array data. Here we select teleseismic earthquake events (located at distances between 30° and 90° from the array center) with moment magnitude Mw > 6.2 recorded by the USArray in the Eastern United States (Figure 2). The crustal structures beneath the Eastern United States are relatively simple compared with the locations of other large regional arrays, for example, Western United States and Europe. Therefore, their interstation coherence patterns are less affected by crustal scattering at the array side. The teleseismic P wave has a nearly vertical incident angle; therefore we only consider vertical-component seismograms with the signal-to-noise ratio (SNR) above 2.5. The SNR is defined here as the ratio of the root mean square amplitude of the signal and noise, measured in 10-s-long windows starting at the P arrival and at 20 s before P arrival, respectively. The array recordings are band-pass filtered in three frequency bands: 0.25–0.5, 0.5–1, and 1–2 Hz. We align the filtered waveforms by cross-correlating their initial P arrivals at each frequency band with a window length of 15, 8, and 6 s, respectively, in order to mitigate the travel time errors due to unmodeled velocity structure. To ensure the robustness of the coherence measurements, we only select events with more than 100 aligned waveform traces. In total, 192 events are incorporated into the analysis, where 127 of them are shallow earthquakes (<70 km), 35 of them are intermediate-depth earthquakes (70–300 km), and 30 of them are deep-focus earthquakes (>300 km). The number of stations for each selected earthquake varies a little but does not affect the aperture of the array too much. The studied earthquakes cover three major subduction zones: the Sea of Okhotsk, Japan, and South America (Figure 2).

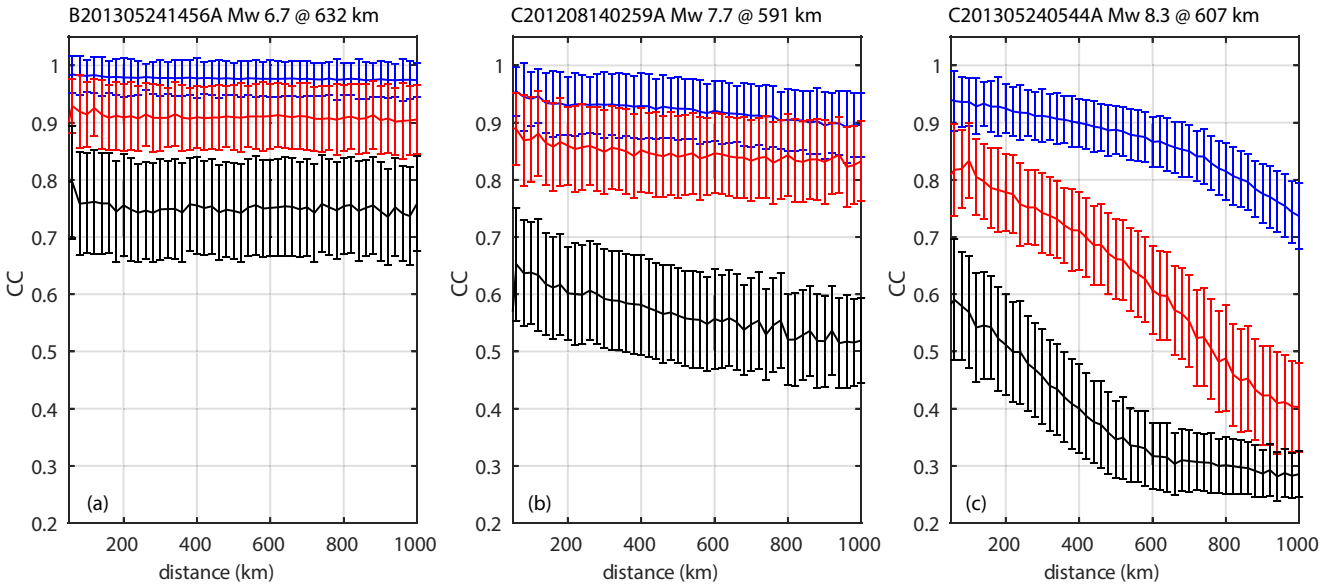

Figure 3. Waveform coherence cross-correlation coefficient (CC) as a function of interstation distance for three deep earthquakes beneath the Sea of Okhotsk recorded by the USArray in the Eastern United States in 3 frequency bands: 0.25–0.5 Hz (blue), 0.5–1 Hz (red), and 1–2 Hz (black).

We computed waveform coherence, in each frequency band, using the normalized cross-correlation coefficient (CC) between all the station pairs defined as

$$\mathrm{CC} = \frac{\int_{t_s}^{t_e} u_1(x_1, t) \cdot u_2(x_2, t)\mathrm{d}t}{\int_{t_s}^{t_e} |u_1(x_1, t)|^2\mathrm{d}t \int_{t_s}^{t_e} |u_2(x_2, t)|^2\mathrm{d}t}, \quad (7)$$

where u_1 and u_2 are the filtered waveforms of two different stations in the time window $[t_s, t_e]$. x_1 and x_2 denote the location of each station related to the hypocenter. The selected time windows start at the initial P arrival and have a duration equal to the source duration according to the global centroid moment tensor (gCMT) catalog (Ekström et al., 2012). Such windows are sufficiently long to record the whole rupture process but short enough to avoid coda waves with low coherence. Each event has on average approximately 20,000 unique station pairs. To statistically quantify the coherence pattern, we group station pairs into bins of interstation distances, with an interval of 50 km, and investigate the median coherence of each bin as a function of interstation distance. For each distance bin, we also report the standard deviation of the median coherence obtained by bootstrapping based on 100 realizations of 85% randomly selected station combinations (Efron & Tibshirani, 1994).

To demonstrate the array coherence patterns, we select three deep earthquakes with depths ranging from 591 to 632 km beneath the Sea of Okhotsk (Figure 2c). The Mw 8.3 Okhotsk earthquake C201305240544A (gCMT event ID) is the largest deep-focus earthquake ever recorded and has been well documented in previous studies including finite source inversions, multiple source inversions, back-projection, and directivity analysis (Chen et al., 2014; Meng et al., 2014; Park & Ishii, 2015; Wei et al., 2013; Ye et al., 2013; Zhan et al., 2014). The Mw 6.7 event B20130524145A occurred near the source region of the Mw 8.3 event, and the Mw 7.7 earthquake C201208140259A occurred in the southern region of the Sea of Okhotsk subduction zone. The duration of the Mw 8.3, 7.7 and 6.7 events, which we set as window duration to measure waveform coherence, are 71, 35 and 11 s, respectively, according to global centroid moment tensor solutions (Ekström et al., 2012). Considering the large epicentral distance to the array (about 60°), the recordings of these events share similar path effects; therefore, coherence differences among them are mainly controlled by source effects.

The Mw 6.7 earthquake has smaller source effects than the other two earthquakes. The coherence for this event (Figure 3a) is above 0.9 in the 0.25–0.5 and 0.5–1 Hz frequency bands. Remarkably, coherence remains high up to interstation distances exceeding 1,000 km. The slow coherence decay with interstation distance suggests that the source effect of this earthquake is small. The baseline coherence in the frequency bands of 0.25–0.5, 0.5–1

and 1–2 Hz is 0.96, 0.92, and 0.78, respectively. The lower coherence at higher frequency is expected due to wave scattering in the 3-D velocity structure.

As the magnitudes (and therefore earthquake rupture sizes) increase, we observe a significant coherence decay as a function of both interstation distance and frequency. In the 0.25–0.5 and 0.5–1 Hz frequency bands, the coherence of the Mw 7.7 earthquake decays about 0.05 over a distance range of 1,000 km. The Mw 8.3 event shows even faster interstation coherence decay, from 0.95 to 0.8 and from 0.8 to 0.4, respectively. In the 1–2 Hz band, the coherence of the Mw 7.7 and Mw 8.3 events decays with interstation distance from 0.65 to 0.5 and from 0.6 to 0.3, respectively.

In principle, the CC value should be 1 at zero interstation distance. However, we measure CC values smaller than 1 at zero distance, especially at higher frequencies (Figure 3). There are two potential explanations: (a) the minimum station interval of the USArray is around 30 km; therefore, our CC values at distance zero are extrapolation and may not capture a possible steeper coherence decay within the first 30 km. (b) The interstation waveform coherence is also affected by the velocity structure right beneath the station site, and spatial variability of site effects can significantly lower the coherence (e.g., one station might be on a rock site and the other is on a nearby sedimentary basin). Such local scattering difference can be described by the 'error difference' term in Equation 6. We also observe in Figure 3 that the CC value at the minimum interstation distance decays with increasing frequency, consistent with the expectation that higher frequency waveforms are more affected by local scatterings and site effects. Given such observation, we choose for our further analysis of source effect the two lower frequency bands, 0.25–0.5 and 0.5–1 Hz. Both frequency bands satisfy the condition that CC > 0.7 at the minimum interstation distance for the Mw 8.3 earthquake. Therefore, they are the highest frequency bands where the scattering due to velocity heterogeneities does not strongly affect the coherence pattern.

4. Constraining Earthquake Dimensions With Coherence Decay Rates

4.1. Earthquake Size Estimation Based on the 1-D Unilateral Haskell's Source Model

From Equation 6, a linear relationship between the arc cosine of CC and the projection difference can be derived:

$$\text{acos(CC)} = \frac{\omega L d_p}{2c} + \delta. \tag{8}$$

Equation 8 shows that acos(CC) scales with projection difference via a factor of $\omega L/2c$. The error difference, δ, is assumed independent on projection difference d_p because the site effects only depend on shallow velocity structures beneath each station, which we treat as stochastic in space. This means δ is nonzero, which leads to acos(CC) < 1 at $d_p = 0$. This again explains why the actual CC measurement is always smaller than 1 at zero interstation distance.

We perform a linear fitting using Equation 8 to find the best $\omega L/2c$ (slope) and δ (intercept) for each earthquake. Figures 4a–4f shows the fitting result of the three deep earthquakes beneath the Sea of Okhotsk in the 0.25–0.5 and 0.5–1 Hz frequency bands. Here, we focus on the slope and estimate the rupture length L. The uncertainty of the fitted slope is derived from the uncertainty of CC measurements (see Section 2.1) using an error propagation theorem (Bevington & Robinson, 2002).

In the two frequency ranges, the data from all three earthquakes satisfy the linear relationship between acos(CC) and projection difference d_p in Equation 8 (Figures 4a–4f). Theoretically, the estimated rupture length should be independent of the measurement frequency band. This is verified for the Mw 8.3 earthquake (Figures 4b and 4e). However, for the Mw 6.7 earthquake, the relatively flat acos(CC) curve suggests that the finite source effect is small, and the source size is difficult to be constrained from the coherence pattern. For small earthquakes, the observed interstation coherence fluctuation is not controlled by finite-source effects, but rather by path effects and array-side scattering, which makes the estimation of rupture length from the array coherence decay rate less robust for small earthquakes. The Mw 7.7 earthquake also shows a discrepancy of the estimated rupture length in two frequency bands. In fact, a complex rupture process including bilateral rupture and low aspect ratio (L/W) can also influence the estimation of rupture length and bring uncertainties. Therefore, the simple model is only suitable for earthquakes with elongated rupture ($L/W \gg 1$). We listed all the linear fitting results for M7+ earthquakes in Figure S1.

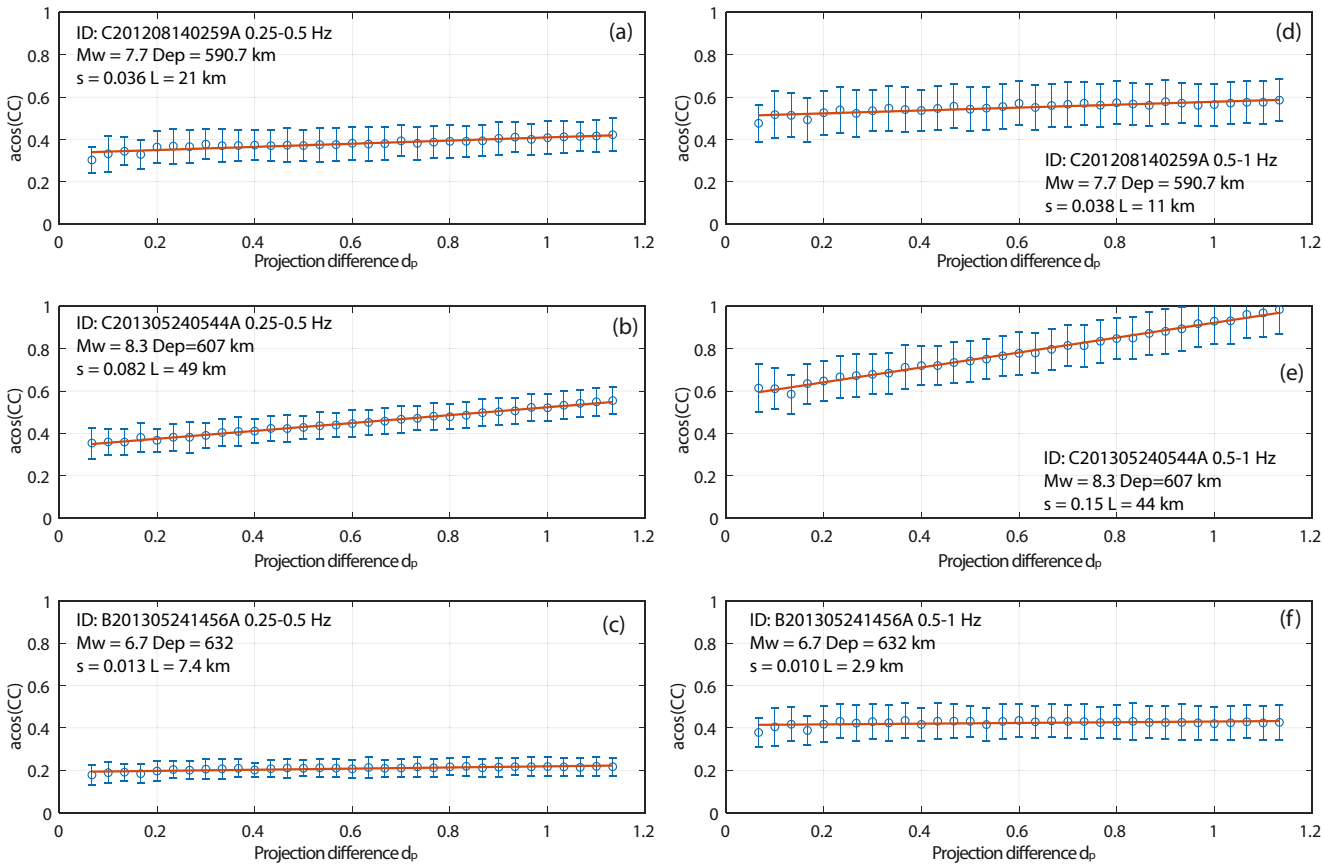

Figure 4. Coherence decay curve as a function of projection difference d_p and the inferred rupture length for the three selected deep earthquakes under the Sea of Okhotsk. Events are labeled with gCMT ID. Two frequency bands are considered: 0.25–0.5 Hz (left columns) and 0.5–1 Hz (right columns). Blue: observations; red: best-fitting lines. In each panel, the slope of the relation between acos(CC) and d_p is indicated as "s" and the estimated rupture length as "L".

We notice that the estimated rupture length L is underestimated. For example, the coherence-based rupture length estimation for the Mw 8.3 earthquake in the Sea of Okhotsk is about 49 km. However, teleseismic back-projection gives a rupture size of around 145 km, comprising a 40-km-long northward propagating segment and a 110-km-long southward propagations (Meng et al., 2014). Finite fault inversion results show even larger rupture length around 195–220 km (Wei et al., 2013; Ye et al., 2013). The interference effect of bilateral rupture fronts underestimates the rupture length by 1/2 (see Section 5.2), resulting a calibrated rupture length estimation of 98 km. The remaining underestimation is possibly caused by the gap between Haskell's rupture model and source complexities, including the aspect ratio (L/W), heterogeneous slip distribution, etc. (see Section 5.2).

4.2. The Moment-Size Scaling Relations

Real earthquakes are far from 1-D Haskell's model, which leads to systematic error of the coherence-measured rupture length. However, the coherence method is still useful because it can capture the order-of-magnitude of the earthquake rupture size, and distinguish different moment-size scaling relations. Here, we analyze the scaling relation between earthquake rupture size inferred from array coherence decay and the moment magnitude. The seismic moment is defined as $M_0 = \mu DA$, where μ is the shear modulus, D the average slip and A the rupture area. Since both D and A depend on rupture size, the moment can be regarded as proportional to a power of rupture size, that is, $M \propto L^n$. Considering the definition of moment magnitude $M_w = (\log M - 9.1)/1.5$, we have

$$\log L \propto \frac{3}{2n} M_w, \tag{9}$$

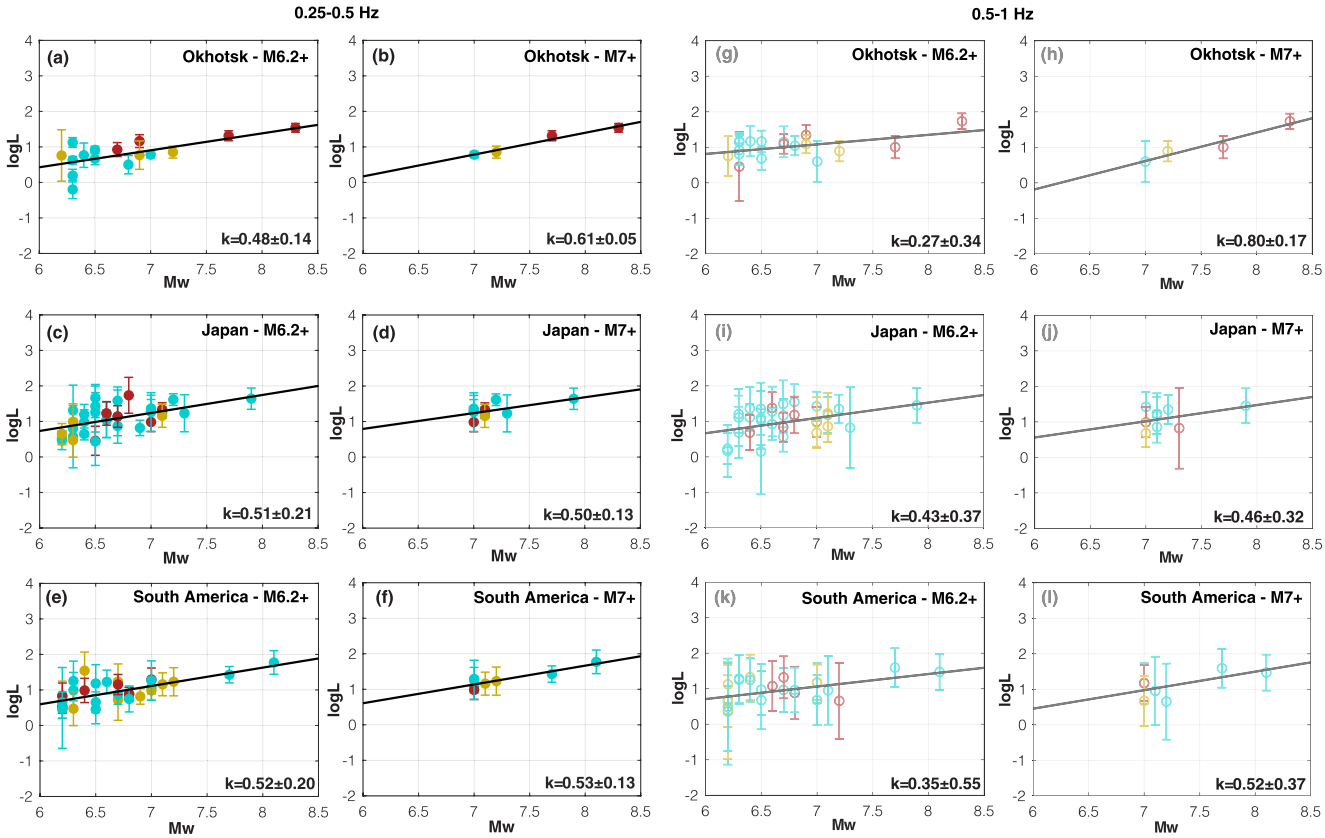

Figure 5. Moment-size scaling relation inferred from the array coherence decay rate of USArray in the Eastern United States. (a–f): in 0.25–0.5 Hz; (g–l): in 0.5–1 Hz. (a, b, g, and k): the Sea of Okhotsk subduction zone; (c, d, i, and j): Japan subduction zone; (e, f, k, and l): South America subduction zone. (a, c, e, g, i, and k): events with Mw > 6.2; (b, d, f, h, j, and l): events with Mw > 7. The *k*-value (slope) of the fitted scaling relation curve *k* is indicated in each subfigure. Colors are coded for different focal depths: blue: shallow earthquakes (<70 km), orange: intermediate earthquakes (70–300 km), and red: deep-focus earthquakes (>300 km). The uncertainty of each earthquake is estimated by the error propagation theory.

Therefore, the logarithm of rupture size has a linear relation with moment magnitude and the slope (*k*-value, $k = 3/2n$) represents the power-law factor of the scaling relation.

We analyze the scaling relation between the coherence-decay estimated log L and moment magnitude in the three study regions: the Sea of Okhotsk, Japan and South America subduction zones (Figure 5). Compared to the measurements showing large error bars in the frequency band of 0.5–1 Hz (Figures 5g–5l), the source size measurements performed in the frequency band of 0.25–0.5 Hz yield more stable estimations (Figures 5a–5f), which is possibly because of even smaller scatterings and path effects. Therefore, we mainly analyze the scaling relations estimated with the frequency band of 0.25–0.5 Hz.

To analyze the effects of moment magnitude ranges on *k*-value, we fit the linear scaling relation between log L and Mw in two magnitude ranges: M6.2+ and M7+. The uncertainties of the rupture size estimation of M7+ earthquakes (the error bars in Figures 5b, 5d and 5f) are generally smaller than M6 class earthquakes (the error bars in Figures 5a, 5c and 5e). Thus, we consider that the *k*-value estimation is more stable for M7+ earthquakes. The coherence-decay estimated rupture size of M6 class earthquakes yields larger uncertainty and scattering because of two factors. First, although the minimum measuring frequency 0.25 Hz is generally above the theoretical first corner frequency of M6+ earthquakes (around 0.1 Hz, Geller (1976)), which enables the observation of finite source effects, the variation of corner frequencies (e.g., in the Japan region, 0.25 Hz, Izutani & Kanamori (2001)) may lead to less observable finite source effects. Second, as discussed earlier, M6 class earthquakes have smaller array coherence decay rates from finite source effects; thus the array coherence decay measurements are more likely to be affected by scatterings and local heterogeneities along the path and at the station side.

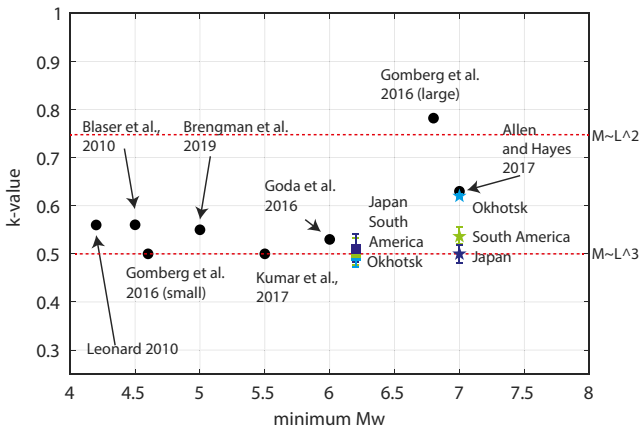

Figure 6. Comparison of the coherence-inferred *k*-values in different regions and *k*-values inferred from other scaling relation studies. Black dots: *k*-values and minimum moment magnitudes of previous scaling relation studies. Squares: coherence-inferred *k*-value for M6 class earthquakes. Stars: coherence-inferred *k*-value for M7+ earthquakes. Squares and stars are color coded by subduction zones. The uncertainty of each earthquake is estimated by the error propagation theory.

We then compare the coherence-inferred *k*-value with previous studies. Theoretically, *k*-value depends on the magnitude range of earthquakes. For large earthquakes (M7+), the rupture width W saturates and two end-member models are possible: the *L*-model with $D \propto L$, implying $n = 2$ and $k = 0.75$, and the *W*-model with $D \propto W$, implying $n = 1$ and $k = 1.5$ (Romanowicz & Rundle, 1993). For smaller earthquakes (M6), which have quasi equal rupture dimensions, $W \propto L$ and $k = 0.5$. Here, we use M7 as an empirical transition magnitude between quasi equal-dimensional and elongated ruptures (Scholz, 2019).

Previous scaling relation studies based on finite-fault inversions, geodetic and geological surveys manifest consistent *k*-value as theoretical models (Allen & Hayes, 2017; Blaser et al., 2010; Brengman et al., 2019; Goda et al., 2016; Gomberg et al., 2016; Leonard, 2010; Thingbaijam et al., 2017) (dots in Figure 6). Most of the measurements of M4–M6 class earthquakes show *k*-values around 0.5 (Blaser et al., 2010; Brengman et al., 2019; Goda et al., 2016; Gomberg et al., 2016; Leonard, 2010; Thingbaijam et al., 2017), suggesting quasi equal-dimensional rupture. For M7 class earthquakes, Gomberg et al. (2016) reported $k = 0.78$, which is close to the *L*-model. However, Allen & Hayes (2017) reported a $k = 0.63$, which is in between the quasi equal-dimensional rupture model and the *L*-model.

The *k*-values estimated by array-coherence decay measurements in the three subduction zones show good consistency with those studies (squares and stars in Figure 6). For M7+ earthquakes, the *k*-value of the Sea of Okhotsk (0.61) is in-between the quasi equal-dimensional model and *L*-model that are compatible with the measurements of other subduction interface earthquakes according to Allen and Hayes (2017). The *k*-values of the Japan and South American subduction zones are around 0.5 (0.53 and 0.50), which is close to the quasi equal-dimensional model. The consistency of the scaling relation derived from array coherence decay indicates that the array coherence decay is a good proxy of rupture size of large earthquakes (Mw > 7). For M6 class earthquakes, the *k*-values of all the three subduction zones are around 0.5, which are close to the quasi equal-dimensional model. The earthquake depth distribution seems not to affect the scaling relation too much, while the magnitude distribution determines the uncertainty of the scaling relation (*k*-value). It is clear that M6.2–M7 earthquakes are highly scattered with large uncertainty in the coherence-measured rupture size. Therefore, the scaling relation (*k*-value) is more accurately estimated for M7+ earthquakes. Since the rupture size estimation for M6–M7 earthquakes have large uncertainties, the *k*-value near 0.5 can only indicate that the coherence roughly constrains the order-of-magnitude of the rupture size.

We argue that M7+ earthquakes are in the transition of two scaling relations of small-magnitude (M6 class, quasi equal-dimensional) and large-magnitude (M7+, $L \gg W$) earthquakes reported by Gomberg et al. (2016); Luo et al. (2017), which is between 0.5 and 0.75. The transition magnitude is related to the seismogenic width W (Luo et al., 2017), which contributes to the variation of *k*-values. Different distributions of seismogenic width controlled by variations of slab geometry and along-dip rheology may also be responsible for regional variation of *k*-values in different subduction zones. Furthermore, the variations of the *k*-value in different subduction zones may be indicators of scale-dependence of rigidity or stress drop (Izutani & Kanamori, 2001), which is related to spatial heterogeneities of the rupture region (Cocco et al., 2016). If the scaling of rigidity or stress drop with rupture size is expressed by $\mu(\Delta\sigma) \propto L^{\alpha}$ (Geller, 1976), then the *k*-value can be expressed by $k = 1.5/(n + \alpha)$. The *k*-value for earthquakes with scale-dependent rigidity or stress drop is smaller than the *k*-value for earthquakes with scale-invariant fault parameters.

The variation of *k*-value between different subduction zones may indicate different transition magnitudes and different scale-dependent source parameters. These properties are further affected by the seismogenic width, geometry/rheological properties along the fault plane, and velocity weakening/strengthening properties related to temperature or subduction materials. For example, the Sea of Okhotsk subduction zone earthquakes show larger *k*-value, which may indicate that the seismogenic width is easy to be saturated. The complex relation between *k*-value variations and subduction zone properties requires further studies.

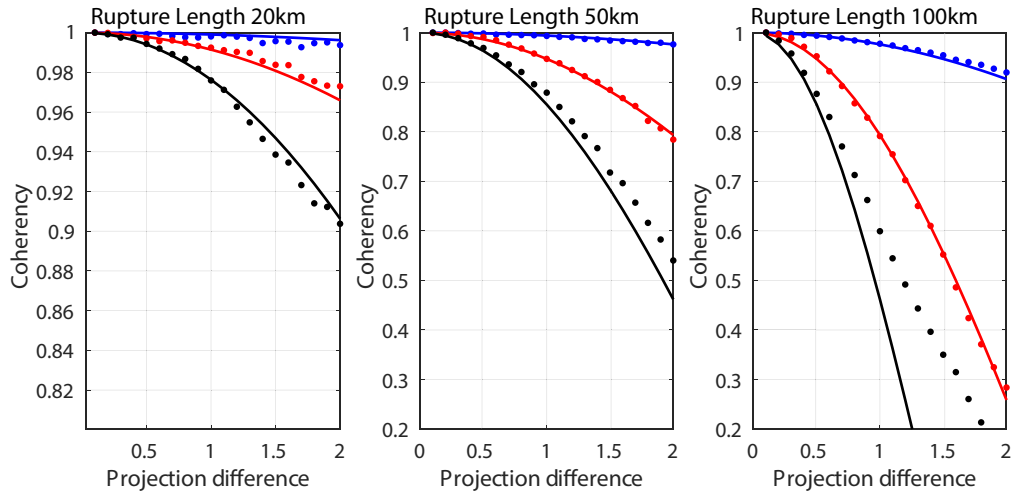

Figure 7. Simulated coherence decay as a function of interstation projection difference. The array is located at 30° from the source. The rupture velocity is assumed to be 3 km/s. We consider three rupture lengths, 20, 50, and 100 km. The coherence pattern is shown in three frequency ranges: 0.25–0.5 Hz (blue), 0.5–1 Hz (red), and 1–2 Hz (black). Dots: coherence computed using narrow-band frequency integration (Equation 3); Solid lines: coherence computed using theoretical monochromatic simulation (Equation 6) in the median frequency (0.375 [blue], 0.75 [red] and 1.5 Hz [black]).

5. Discussion

Here, we analyze the uncertainties of the coherence-based rupture size estimation method in different aspects, including finite frequency, earthquake source complexities including the aspect ratio of earthquake rupture, bilateral rupture, etc. We also give our prospective of this unique coherence-based earthquake rupture size estimation method and the possible future applications.

5.1. Finite-Frequency Effects

Note that Equation 6 is valid for monochromatic waves. Therefore, in the coherence measurement with array recordings, the data is filtered in a narrow frequency band. The complete form of the coherence equation requires a weighted integral of Equation 3 over the frequency range of interest, which does not have an analytical form. To examine the possible finite difference effects, we compute the array coherence of the elongated rupture model for various source sizes using the narrow-band integration (Equation 3) in three frequency bands (0.25–0.5, 0.5–1, and 1–2 Hz) and theoretical monochromatic simulation (Equation 6) in the median frequency of the three frequency bands (i.e., 0.375, 0.75, and 1.5 Hz) (Figure 7). The resulting coherence pattern shows the features anticipated from the estimation of the Sea of Okhotsk earthquakes: it decreases monotonically as a function of projection difference; it decays faster at higher frequencies; and for a given frequency range, a larger rupture length results in faster coherence decay. Besides, in the two lower frequency bands (0.5–0.25 and 0.5–1 Hz, also the two selected frequency ranges for further analysis), the coherence patterns are consistent between numerical narrow-band integration and theoretical monochromatic simulation. The coherence pattern for projection differences up to 2° is almost identical, especially for large rupture lengths (>100 km) (Figure 7). There are notable difference between the monochromatic simulation and narrow-band integration in 1–2 Hz for the rupture length of 100 km due to finite frequency effects.

5.2. Effects of Source Complexity on Rupture Size Estimation

Since we apply a unilateral 1-D rupture model to fit the array coherence decay function, deviation from this rupture model may induce uncertainties in the rupture size estimation. Kinematic rupture properties, such as the different aspect ratio (L/W), bilateral versus unilateral rupture propagation, and variation of rupture speeds, are expected to introduce additional complexities.

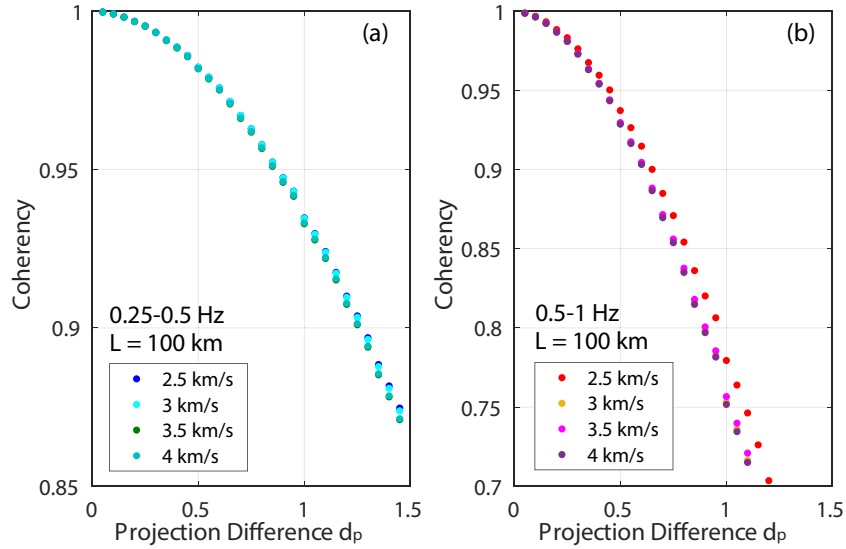

Figure 8. Simulated coherence pattern for an elongated Haskell's source model with different rupture speeds (2.5, 3, 3.5 and 4.5 km/s). Coherence is presented as a function of projection difference d_p. Rupture length is assumed to be 100 km. Station and fault settings are the same as Figure 7. (a) coherence pattern in 0.25–0.5 Hz; (b) coherence pattern in 0.5–1 Hz.

5.2.1. Rupture Speed

Rupture speed is eliminated in monochromatic Equation 6; however the complete form of integrating Equation 3 over the frequency range will introduce second-order terms involving the rupture speed. We conduct a synthetic test to demonstrate the effect of the rupture speed in our selected narrow frequency bands (Figure 8). The rupture length is assumed to be 100 km. In the frequency bands of 0.25–0.5 and 0.5–1 Hz, the effect of rupture speed is minor since the coherence decay pattern is nearly identical for rupture speed of 2.5, 3, 3.5 and 4 km/s (Figure 8). The maximum deviation of the CC value at projection difference of 1° is only 0.0019 and 0.027 for 0.25–0.5 Hz and 0.5–1 Hz, respectively, which correlates to the rupture length deviation of 0.1 and 1.6 km, respectively. The nearly identical coherence pattern ensures little uncertainty in the estimation of rupture size in the two narrow frequency ranges.

5.2.2. Rupture Aspect Ratios

The rupture aspect ratio also influences the uncertainty of rupture length estimates from array coherence decay rates. Since we assume $L \gg W$, the main rupture direction is along the strike and the waveform coherence is only influenced by a series of 1-D rupture patches (Equation 5). 2-D rupture effects are not negligible when considering a rupture with a lower aspect ratio. In such cases, the rupture direction is not along the strike and the teleseismic waveform consists of multiple components from 2-D fault patches. The coherence pattern is therefore more complex and does not have an explicit form. Here, we further consider a 2-D rupture model to analyze the effects of the rupture aspect ratio L/W on the array coherence approach. The teleseismic wavefield of a 2-D Haskell's source model is

$$u(r,\phi,t) = \frac{\mu}{4\pi\rho c^3}\int_0^L\int_0^W \frac{R}{r}\dot{D}\left(t - \frac{r}{c} - \frac{x}{V_{rx}} - \frac{y}{V_{ry}} + \frac{\sqrt{x^2+y^2}\cos\phi\,\sin\theta}{c}\right)\mathrm{dxdy}, \tag{10}$$

where $1/V_{rx}$ and $1/V_{ry}$ are the components of the rupture slowness vector along the x (rupture length L) and y (rupture width W) directions, respectively. The seismic recording at a station is now a surface integral along the rupture area. Equation 10 does not have analytical solutions for a general case; so we conduct numerical simulations to demonstrate the effects of rupture complexity. To simplify the simulation, we assume that the rupture width W is constant, such that $L \gg W$. Under this assumption we integrate Equation 10 and get the far-field monochromatic wavefield as

$$u(\omega,T) = \frac{\mu RW}{4\pi\rho c^3 r}\dot{D}(\omega)e^{-\frac{i\omega r}{c}}\left(H_z e^{-iZ} + H_Y e^{-iY}\right) \tag{11}$$

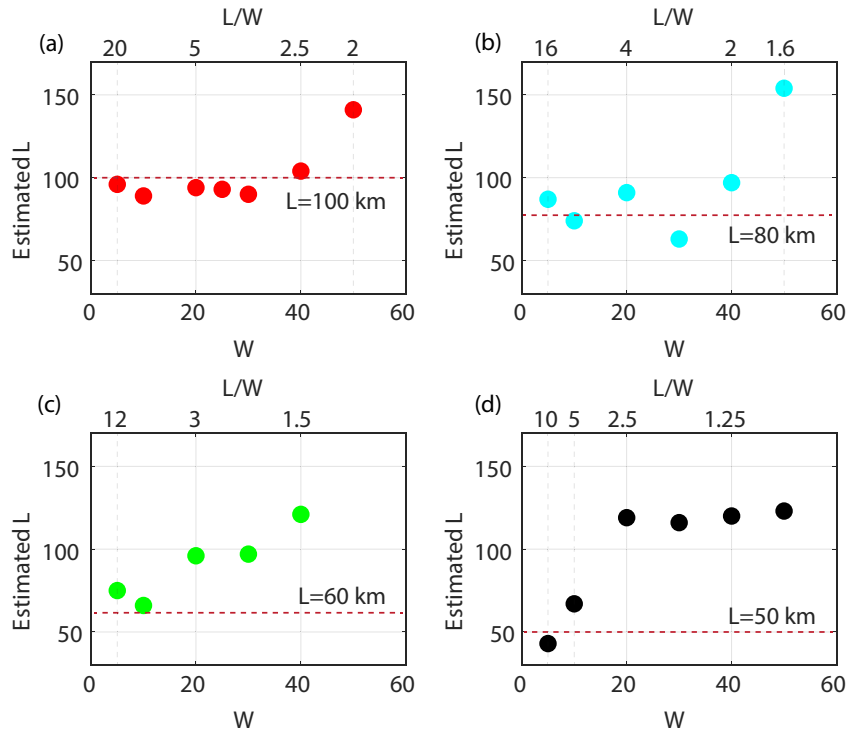

Figure 9. The effect of the aspect ratio (L/W) on coherence estimated rupture size in 0.25–0.5 Hz frequency band. (a–d) are tested with true rupture length of 100, 80, 60, and 50 km, respectively. The rupture velocity is assumed to be 3 km/s. Coherence estimated rupture length is plotted as a function of rupture width W (bottom axis) and corresponding aspect ratio L/W (top axis). Red dashed lines indicate the true rupture length.

where $Z = \omega L/2*(1/V_{rx} - \sin\theta\cos\phi/c)$, and $Y = \omega L/2*(1/V_{ry} + \sin\theta\cos\phi/c)$. $H(Z)$ and $H(Y)$ are the sinc functions of Z and Y, respectively.

We conduct a synthetic test using different rupture lengths and different aspect ratios in 0.25–0.5 Hz (Figure 9) to test the valid L/W range in which our assumption of elongated rupture applies. We find larger ruptures generally allow a lower valid L/W ratio than smaller ruptures. If we consider that 20% uncertainty of the rupture length is acceptable, L/W needs to be greater than 5 for $L = 50$ km but can be as low as 2.5 for $L = 100$ km. The lower threshold of the valid L/W ratio for larger events may explain why the array coherence decay rate estimation is more suitable for large earthquakes (Mw > 7).

5.2.3. Bilateral Ruptures

A bilateral rupture case is also a deviation from the unilateral rupture assumed in Equation 5. To simplify the analysis, we consider a symmetric bilateral rupture with rupture length L, which can be regarded as the sum of two unilateral ruptures of length $L/2$ propagating in opposite directions simultaneously. Theoretically, the relation between coherence and projection difference is

$$\text{acos(CC)} = \frac{\omega L d_p}{4c} + \delta, \tag{12}$$

The denominator of the first term on the right-hand side in Equation 12 is 4c, instead of 2c in Equation 8. Thus a symmetric 1-D bilateral rupture reduces the interstation coherence decay rate by 1/2. Therefore, for a symmetric bilateral rupture, the estimated length assuming a unilateral rupture is half the true length. An example is the 2013 M8.3 Sea of Okhotsk earthquake. Based on back-projection and finite-fault inversions (Meng et al., 2014; Wei et al., 2013; Ye et al., 2013), this earthquake has two rupture branches propagating northeastward and southwestward, respectively. The coherence-based rupture length estimation is 49 km. If considering the bilateral rupture correction, the estimated rupture length will be 98 km, which is closer and within one order of magnitude of the

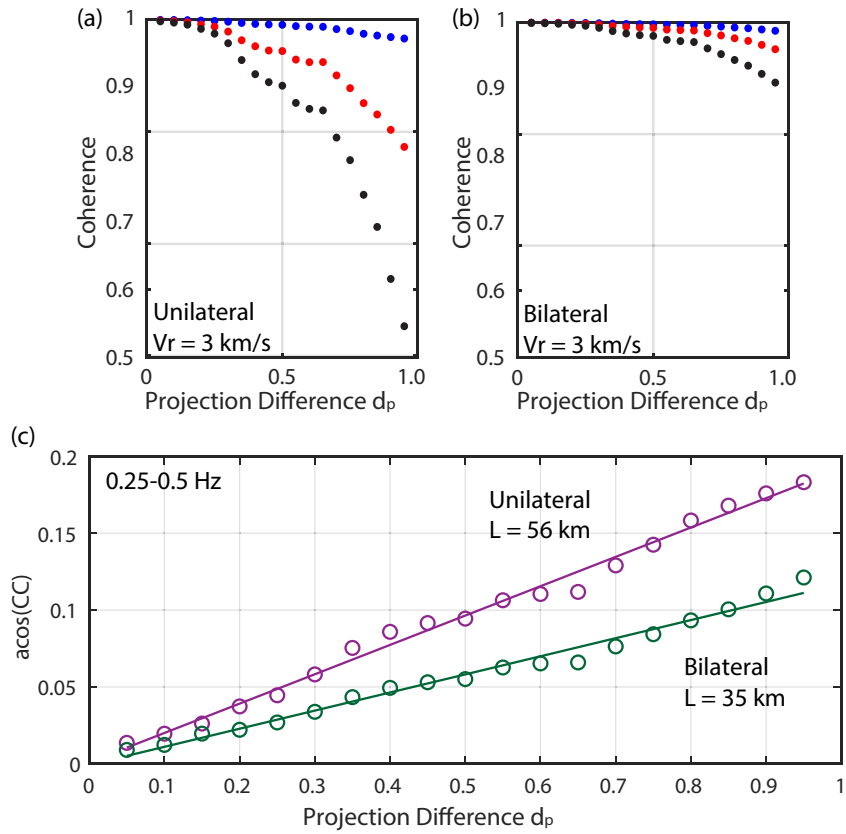

Figure 10. Coherence decay curve as a function of projection difference d_p for 2-D unilateral and bilateral ruptures and the corresponding rupture length estimates. (a) unilateral rupture; (b) bilateral rupture. Three frequency bands are color coded with blue (0.25–0.5 Hz), red (0.5–1 Hz), and black (1–2 Hz). The rupture dimension is set as 10 km along dip and 50 km along strike. The rupture speed is set as 3 km/s. Synthetic coherence are computed using Equation 11. (c) rupture size estimation in 0.25–0.5 Hz for coherence decay curves (a and b). Unilateral rupture and bilateral rupture are color coded by purple and dark green, respectively. The rupture length estimation is using 1-D model (Equation 8).

back-projection estimated rupture length of 145 km. There is still underestimation of the rupture size, partially because this earthquake has a complex rupture process with multiple rupture branches.

More realistic bilateral rupture models can be described with a 2-D rupture. Here, we conduct a synthetic test of a $W{*}L = 10{*}50$ km rupture dimension for both the unilateral and bilateral ruptures using Equation 11 (Figures 10a–10d). The pattern of coherence decay with projection difference deviates from the cosine-shaped function for projection difference larger than 0.5 and the coherence decay is faster compared to 1-D rupture model. Bilateral rupture is also observed to reduce the coherence decay rate. For example, with a rupture speed of 2.5 km/s, the coherence estimated rupture length in the 0.25–0.5 Hz frequency band is 56 km for a unilateral rupture and 35 km for the bilateral rupture. Rupture size estimation using a 1-D source model for bilateral rupture will lead to a rupture size underestimation of 30%. Theoretically, one could estimate the rupture size using a bilateral rupture model or a 2-D rupture model with inversion methods. However, bilateral ruptures in reality are hardly symmetric, which cannot be expressed in an explicit form for estimating the rupture length directly. Moreover, interference between the two rupture fronts create extra waveform complexities that add much uncertainty to the array coherence measurement. Therefore in this paper, while we analyze and discuss the effects of bilateral ruptures, we still apply an elongated unilateral rupture model to examine the rupture lengths.

The coherence measured rupture size may be more representative of the main asperity than the entire rupture. Large earthquakes usually show slip heterogeneities (Brown et al., 2015), where multiple areas of large slip are separated by small slip patches, acting as asperities or sub-sources. Since the assumption of our coherence method is based on waveforms generating from a continuous rupture area, the main asperity of a large earthquake

may take control of the waveform coherence. Therefore, the underestimation of the rupture size of certain large earthquakes (e.g., the M8.3 Sea of Okhotsk) may be caused by slip heterogeneity.

5.3. Future Work of the Coherence Based Source Analysis

We observe a salient feature that the array coherence decay rate depends on earthquake source size. A simple analytical relation, under the assumption of an elongated Haskell's source model, is able to explain that the coherence behavior is generally governed by the earthquake source size. We further develop a method to measure source size from the coherence curve, assuming a simple unilateral rupture model. The method can give an approximate estimation for fault rupture sizes for the main asperity. For deep and oceanic earthquakes, where satellite geodesy is unavailable, source dimension is conventionally inferred from finite-fault source inversion or back-projection. Teleseismic-only finite-fault inversions generally suffer from nonuniqueness due to trade-off between source size and rupture speed. Back-projection can generally map the trajectory of the rupture, but coda waves and scatterings can generate uncertainties in determining when the earthquake stops, which adds uncertainty to the rupture size. Hence, estimated source sizes are subject to large variabilities. We can utilize the coherence curve as an alternative to cross-validate the inferred source size. If the estimated size is close to the true size, the synthetic coherence curve should match the observation. The observation of the relation between the array coherence decay rate and earthquake rupture size also potentially provides additional constraints to discriminate physical models of subduction zone earthquakes derived from numerical simulations and laboratory experiments.

6. Conclusion

In this study, we report a new observation of the relation between earthquake rupture size and the decay rate of interstation waveform coherence as a function of projection difference within a seismic array. We observe that coherence is predominantly modulated by source size for large earthquakes (Mw > 7) in the frequencies above the earthquake's corner frequency; it decays faster if the source size is larger. Increasing the source size causes a larger interstation difference of phase delays between seismic waves from different parts of the source, resulting in a breakdown of waveform coherence. Assuming a simple elongated Haskell's source model, the array coherence decay can be used to roughly estimate the rupture size L. The inferred rupture size satisfies empirical scaling relations between rupture length and moment magnitude. Furthermore, our estimation shows that the scaling exponent between rupture length and magnitude of large earthquakes (Mw > 7) is in between 0.5 and 0.75 for several subduction zones, which corresponds to the transition from the quasi equal-dimensional source model and the L-model. Despite the uncertainties coming from rupture aspect ratio, bilateral rupture, and structural heterogeneities, our proposed method has the potential to cross-validate source sizes from other studies and to fill the gap of rupture size estimation for deep and remote earthquakes.

Appendix A: Derivation of Equation 6

We start from the definition of the cross-correlation coefficient in the frequency domain:

$$CC(\omega) = \frac{\mathrm{Real}(U(S_A, \omega) \cdot U^*(S_B, \omega))}{|U(S_A, \omega)| \cdot |U(S_B, \omega)|}. \tag{A1}$$

Substituting Equation 5, the numerator of cross-correlation coefficient (CC) is

$$\mathrm{NUM} = \mathrm{Real}(U(S_A, \omega) \cdot U^*(S_B, \omega)) = C_{AB} \exp\left[-i\omega\left(\frac{r_A - r_B}{c} + \frac{L(S_A - S_B)}{2} + g_A - g_B\right)\right], \tag{A2}$$

where

$$C_{AB} = \frac{\mu^2 R^2 W^2 G_A G_B}{16\pi^2 \rho^2 c^6 r_A r_B} \dot{D}^2(\omega) \frac{1}{\omega^2 S_A S_B} \sin\left(\frac{\omega L}{2} S_A\right) \sin\left(\frac{\omega L}{2} S_B\right). \tag{A3}$$

Using the Euler's formula and taking the real part, we get

$$\mathrm{NUM} = C_{AB} \cos\left[\omega\left(\frac{r_A - r_B}{c} + \frac{L(S_A - S_B)}{2} + g_A - g_B\right)\right]. \tag{A4}$$

Substituting Equation 5 in the denominator of CC, we get

$$\mathrm{DEN} = |U(S_A, \omega)| \cdot |U(S_B, \omega)| = C_{AB}\sqrt{\left|\exp\left[-i\omega\left(\frac{r_A}{c} + \frac{LS_A}{2} + g_A\right)\right]\right|^2} \cdot \sqrt{\left|\exp\left[-i\omega\left(\frac{r_B}{c} + \frac{LS_B}{2} + g_B\right)\right]\right|^2}. \tag{A5}$$

Given that

$$|\exp(-i\theta)|^2 = (\cos\theta)^2 + (-\sin\theta)^2 = 1, \tag{A6}$$

Equation A5 is reduced to

$$\mathrm{DEN} = C_{AB} \cdot \sqrt{1} \cdot \sqrt{1} = C_{AB}. \tag{A7}$$

Next, dividing the numerator (Equation A4) by the denominator (Equation A7), we get

$$\mathrm{CC} = \cos\left[\omega\left(\frac{r_A - r_B}{c} + \frac{L(S_A - S_B)}{2} + g_A - g_B\right)\right]. \tag{A8}$$

Here, the first term $(r_A - r_B)/c$ is the travel time difference from the epicenter to the two different stations A and B. Since we aligned the waveform by the first P arrival, this term can be eliminated. The CC value only depends on the second and third terms which are related to the source size $(L(S_A - S_B)/2)$ and the difference between local path and site effects $(g_A - g_B)$. Substituting the definition of the slowness term $S = 1/V_r - \gamma/c$ (Equation 4), we get

$$\mathrm{CC} = \cos\left[-\frac{\omega L}{2c}(\gamma_A - \gamma_B) + \omega(g_A - g_B)\right] \tag{A9}$$

which is Equation 6.

Data Availability Statement

Our broadband earthquake data set is obtained from FDSN (https://www.fdsn.org) downloaded using ObsPy (https://github.com/obspy/obspy/wiki). The networks used are TA (IRIS Transportable Array (2003), USArray Transportable Array, International Federation of Digital Seismograph Networks. https://doi.org/10.7914/SN/TA), IU (Albuquerque Seismological Laboratory (ASL)/USGS (1988), Global Seismograph Network (GSN - IRIS/USGS), International Federation of Digital Seismograph Networks (https://doi.org/10.7914/SN/IU), II (Scripps Institution of Oceanography) (1986), IRIS/IDA Seismic Network, International Federation of Digital Seismograph Networks (https://doi.org/10.7914/SN/II), US (Albuquerque Seismological Laboratory (ASL)/USGS (1990), United States National Seismic Network, International Federation of Digital Seismograph Networks. https://doi.org/10.7914/SN/US), and AK (Alaska Earthquake Center, U. O. A. F. (1987), Alaska Regional Network, and International Federation of Digital Seismograph Networks (https://doi.org/10.7914/SN/AK). We are grateful to the Global Centroid Moment Tensor Catalog (https://www.globalcmt.org/) for the earthquake catalog with moment tensor solutions.

Acknowledgments
This research was supported by NSF EAR-1848486 and by the Leon and Joann V. C. Knopoff Fund.

References

Aki, K., & Richards, P. G. (2002). *Quantitative seismology*.
Allen, T. I., & Hayes, G. P. (2017). Alternative rupture-scaling relationships for subduction interface and other offshore environments. *Bulletin of the Seismological Society of America*, *107*(3), 1240–1253. https://doi.org/10.1785/0120160255
Bevington, P. R., & Robinson, D. K. (2002). *Data reduction and error analysis for the physical sciences* (3rd ed.). McGraw-Hill.
Blaser, L., Krüger, F., Ohrnberger, M., & Scherbaum, F. (2010). Scaling relations of earthquake source parameter estimates with special focus on subduction environment. *Bulletin of the Seismological Society of America*, *100*(6), 2914–2926. https://doi.org/10.1785/0120100111
Brengman, C. M., Barnhart, W. D., Mankin, E. H., & Miller, C. N. (2019). Earthquake-scaling relationships from geodetically derived slip distributions. *Bulletin of the Seismological Society of America*, *109*(5), 1701–1715. https://doi.org/10.1785/0120190048
Brown, L., Wang, K., & Sun, T. (2015). Static stress drop in the mw 9 Tohoku-oki earthquake: Heterogeneous distribution and low average value. *Geophysical Research Letters*, *42*(24), 10–595. https://doi.org/10.1002/2015gl066361
Burdick, S., Vernon, F. L., Martynov, V., Eakins, J., Cox, T., & Tytell, J. (2017). Model update May 2016: Upper-mantle heterogeneity beneath North America from travel-time tomography with global and USarray data. *Seismological Research Letters*, *88*(2A), 319–325. https://doi.org/10.1785/0220160186

Chen, Y., Wen, L., & Ji, C. (2014). A cascading failure during the 24 May 2013 great Okhotsk deep earthquake. *Journal of Geophysical Research: Solid Earth*, *119*(4), 3035–3049. https://doi.org/10.1002/2013jb010926

Cocco, M., Tinti, E., & Cirella, A. (2016). On the scale dependence of earthquake stress drop. *Journal of Seismology*, *20*(4), 1151–1170. https://doi.org/10.1007/s10950-016-9594-4

Efron, B., & Tibshirani, R. J. (1994). *An introduction to the bootstrap*. CRC Press.

Ekström, G., Nettles, M., & Dziewoński, A. (2012). The global CMT project 2004–2010: Centroid-moment tensors for 13,017 earthquakes. *Physics of the Earth and Planetary Interiors*, *200*, 1–9. https://doi.org/10.1016/j.pepi.2012.04.002

Geller, R. J. (1976). Scaling relations for earthquake source parameters and magnitudes. *Bulletin of the Seismological Society of America*, *66*(5), 1501–1523.

Gibbons, S. J., & Ringdal, F. (2006). The detection of low magnitude seismic events using array-based waveform correlation. *Geophysical Journal International*, *165*(1), 149–166. https://doi.org/10.1111/j.1365-246x.2006.02865.x

Goda, K., Yasuda, T., Mori, N., & Maruyama, T. (2016). New scaling relationships of earthquake source parameters for stochastic tsunami simulation. *Coastal Engineering Journal*, *58*(3), 1650010–1650011. https://doi.org/10.1142/s0578563416500108

Gomberg, J., Wech, A., Creager, K., Obara, K., & Agnew, D. (2016). Reconsidering earthquake scaling. *Geophysical Research Letters*, *43*(12), 6243–6251. https://doi.org/10.1002/2016gl069967

Haskell, N. (1964). Total energy and energy spectral density of elastic wave radiation from propagating faults. *Bulletin of the Seismological Society of America*, *54*(6A), 1811–1841. https://doi.org/10.1785/bssa05406a1811

Hawthorne, J., & Ampuero, J.-P. (2018). A phase coherence approach to identifying co-located earthquakes and tremor. *Geophysical Journal International*, *209*(2), 623–642.

Hawthorne, J., Thomas, A., & Ampuero, J.-P. (2019). The rupture extent of low frequency earthquakes near parkfield, ca. *Geophysical Journal International*, *216*(1), 621–639. https://doi.org/10.1093/gji/ggy429

Ide, S. (2007). Dynamic rupture propagation on a 2D fault with fractal frictional properties. *Earth Planets and Space*, *59*(10), 1099–1109. https://doi.org/10.1186/bf03352053

Izutani, Y., & Kanamori, H. (2001). Scale-dependence of seismic energy-to-moment ratio for strike-slip earthquakes in Japan. *Geophysical Research Letters*, *28*(20), 4007–4010. https://doi.org/10.1029/2001gl013402

Ji, C., Wald, D. J., & Helmberger, D. V. (2002). Source description of the 1999 hector mine, California, earthquake, part i: Wavelet domain inversion theory and resolution analysis. *Bulletin of the Seismological Society of America*, *92*(4), 1192–1207. https://doi.org/10.1785/0120000916

Kiser, E., & Ishii, M. (2017). Back-projection imaging of earthquakes. *Annual Review of Earth and Planetary Sciences*, *45*(1), 271–299. https://doi.org/10.1146/annurev-earth-063016-015801

Langston, C. A. (2014). Coherence of teleseismic P and S waves across the transportable array. *Bulletin of the Seismological Society of America*, *104*(5), 2253–2265. https://doi.org/10.1785/0120140075

Leonard, M. (2010). Earthquake fault scaling: Self-consistent relating of rupture length, width, average displacement, and moment release. *Bulletin of the Seismological Society of America*, *100*(5A), 1971–1988. https://doi.org/10.1785/0120090189

Lin, F.-C., Li, D., Clayton, R. W., & Hollis, D. (2013). High-resolution 3D shallow crustal structure in long beach, California: Application of ambient noise tomography on a dense seismic array. *Geophysics*, *78*(4), Q45–Q56. https://doi.org/10.1190/geo2012-0453.1

Luo, Y., Ampuero, J.-P., Miyakoshi, K., & Irikura, K. (2017). Surface rupture effects on earthquake moment-area scaling relations. *Pure and Applied Geophysics*, *174*(9), 3331–3342. https://doi.org/10.1007/s00024-017-1467-4

Meng, L., Ampuero, J.-P., & Bürgmann, R. (2014). The 2013 Okhotsk deep-focus earthquake: Rupture beyond the metastable olivine wedge and thermally controlled rise time near the edge of a slab. *Geophysical Research Letters*, *41*(11), 3779–3785. https://doi.org/10.1002/2014gl059968

Meng, L., Bao, H., Huang, H., Zhang, A., Bloore, A., & Liu, Z. (2018). Double pincer movement: Encircling rupture splitting during the 2015 mw 8.3 illapel earthquake. *Earth and Planetary Science Letters*, *495*, 164–173. https://doi.org/10.1016/j.epsl.2018.04.057

Mordret, A., Brenguier, F., Causse, M., Boué, P., Voisin, C., Dumont, I., et al. (2020). Seismic stereometry reveals preparatory behavior and source kinematics of intermediate-size earthquakes. *Geophysical Research Letters*, *47*(17), e2020GL088563. https://doi.org/10.1029/2020gl088563

Obara, K. (2012). New detection of tremor triggered in Hokkaido, northern Japan by the 2004 Sumatra–Andaman earthquake. *Geophysical Research Letters*, *39*(20), 2012GL053339. https://doi.org/10.1029/2012gl053339

Park, S., & Ishii, M. (2015). Inversion for rupture properties based upon 3-D directivity effect and application to deep earthquakes in the sea of Okhotsk region. *Geophysical Journal International*, *203*(2), 1011–1025. https://doi.org/10.1093/gji/ggv352

Peng, Z., & Zhao, P. (2009). Migration of early aftershocks following the 2004 parkfield earthquake. *Nature Geoscience*, *2*(12), 877–881. https://doi.org/10.1038/ngeo697

Poli, P., Thomas, C., Campillo, M., & Pedersen, H. A. (2015). Imaging the D" reflector with noise correlations. *Geophysical Research Letters*, *42*(1), 60–65. https://doi.org/10.1002/2014gl062198

Riahi, N., & Gerstoft, P. (2015). The seismic traffic footprint: Tracking trains, aircraft, and cars seismically. *Geophysical Research Letters*, *42*(8), 2674–2681. https://doi.org/10.1002/2015gl063558

Romanowicz, B., & Rundle, J. B. (1993). On scaling relations for large earthquakes. *Bulletin of the Seismological Society of America*, *83*(4), 1294–1297. https://doi.org/10.1785/bssa0830041294

Scholz, C. H. (2019). *The mechanics of earthquakes and faulting*. Cambridge University Press.

Shelly, D. R., Beroza, G. C., & Ide, S. (2007). Non-volcanic tremor and low-frequency earthquake swarms. *Nature*, *446*(7133), 305–307. https://doi.org/10.1038/nature05666

Shen, W., & Ritzwoller, M. H. (2016). Crustal and uppermost mantle structure beneath the United States. *Journal of Geophysical Research: Solid Earth*, *121*(6), 4306–4342. https://doi.org/10.1002/2016jb012887

Thingbaijam, K. K. S., Martin Mai, P., & Goda, K. (2017). New empirical earthquake source-scaling laws. *Bulletin of the Seismological Society of America*, *107*(5), 2225–2246. https://doi.org/10.1785/0120170017

Wei, S., Helmberger, D., Zhan, Z., & Graves, R. (2013). Rupture complexity of the mw 8.3 sea of Okhotsk earthquake: Rapid triggering of complementary earthquakes? *Geophysical Research Letters*, *40*(19), 5034–5039. https://doi.org/10.1002/grl.50977

Ye, L., Lay, T., Kanamori, H., & Koper, K. D. (2013). Energy release of the 2013 mw 8.3 sea of Okhotsk earthquake and deep slab stress heterogeneity. *Science*, *341*(6152), 1380–1384. https://doi.org/10.1126/science.1242032

Zerva, A., & Zervas, V. (2002). Spatial variation of seismic ground motions: An overview. *Applied Mechanics Reviews*, *55*(3), 271–297. https://doi.org/10.1115/1.1458013

Zhan, Z., Kanamori, H., Tsai, V. C., Helmberger, D. V., & Wei, S. (2014). Rupture complexity of the 1994 Bolivia and 2013 sea of Okhotsk deep earthquakes. *Earth and Planetary Science Letters*, *385*, 89–96. https://doi.org/10.1016/j.epsl.2013.10.028